Journal of Structural Geology, Vol. 12, No. 3, pp. 297 to 302, 1990
Printed in Great Britain

0191-8141/90 $03.00+0.00

Effect of ramp geometry on deformation in a ductile décollement level

A. TABOADA, J. F. RITZ and J. MALAVIEILLE

Laboratoire de Tectonique, Université des Sciences et Techniques du Languedoc, Place E. Bataillon, 34095 Montpellier Cédex 5, France

(*Received* 15 *March* 1989; *accepted in revised form* 30 *October* 1989)

Abstract—A theoretical model is presented to explain the relation between the different strain regimes in a ductile décollement level and the ramp geometry. This model accounts for a simple shear regime in the basal flat level and a less rotational and more flattening strain regime along the ramp. The model is applied to a field example where the ramp dip and the shear value on the basal flat are estimated from pressure shadow data.

INTRODUCTION

WHEN sedimentary rocks presenting high ductility contrasts are submitted to compression, deformation is characterized by thrust faults displaying a flat and ramp geometry (Boyer & Elliott 1982, Butler 1982, Mitra 1986). These thrusts propagate through competent beds (ramps), and least resistant levels (flats), following a staircase trajectory (Eisenstadt & De Paor 1987). In this paper we will focus on the deformation of a ductile layer, localized at the base of a sedimentary sequence (Fig. 1). Décollements are generally localized in weak horizons and may show a ductile deformation that affects an important thickness of plastic material (Davis & Engelder 1985). This is the case, for instance, in the external French Alps, where intense shear occurred in Triassic rocks (Gèze 1960, Lemoine 1972). Recent studies have shown that the deformation pattern in these evaporitic plastic horizons is well organized and shows structures consistent with progressive ductile shear: mylonitic foliation, stretching lineation, 'a'-type folds, sheath folds and asymmetrical pressure shadows (Marcoux *et al.* 1987, Ritz & Malavieille 1988).

Moreover, numerical simulation of pressure shadows around rigid objects included in the deformable matrix of the ductile level (Malavieille *et al.* 1982, Etchecopar & Malavieille 1987) showed that the deformation mechanism beyond the basal flat differs from simple shear (Malavieille & Ritz 1989). Deformation in the ductile horizon, where it has moved up a ramp, shows more flattening and less rotation than in the simple shear assumed for the basal flat. The model we present is consistent with the change of strain regime along the décollement, deduced from simulated pressure shadows observed in the ramp. Thus, the dip of the ramp and the shear strain on the basal flat can be calculated from pressure shadow data.

The model has been applied first, using a simple theoretical example in which the ramp dips at 45° (Fig. 1), and then for a field example. In both cases, the initial state of the plastic level is represented by a rectangular element grid which deforms with time.

FORMULATION OF THE MODEL

Lagrange variables (Germain 1986) are used to describe the kinematics of the décollement level. The displacement field in each part of the plastic level is described by linear equation (1), in which variables are referred to a local frame of reference (Fig. 2a). The different parameters are given in Table 1.

$$x(t)_i = D(t)_{ij}X(t_0)_j, \qquad (1)$$

where $x(t)_i$ represents the final co-ordinates at time t of a material point, whose initial position in the undeformed state at time t_0, is given by $X(t_0)_j$. Matrix coefficients $D(t)_{ij}$ are independent of position.

To simplify the equations, we have chosen a simple theoretical case in which the deformation of the ductile horizon satisfies the following constraints: (a) plane strain and constant area, which implies that $\mathrm{Det}\cdot[D(t)] = 1$; and (b) homogeneous deformation in

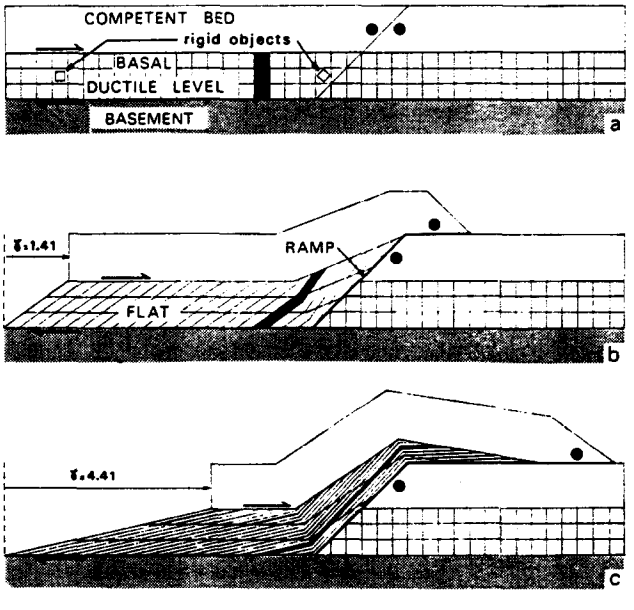

Fig. 1. Sketch showing deformation of a grid representing a ductile décollement level, for different shear values (the thickness of the basal ductile level has been exaggerated).

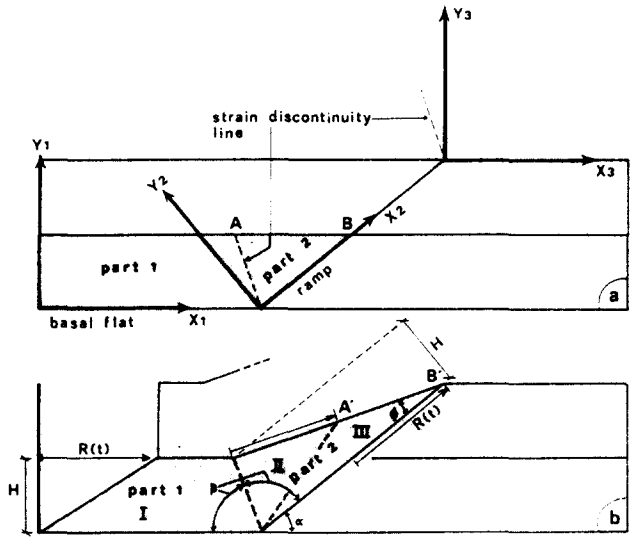

Fig. 2. Geometrical description of the décollement level. (a) Initial state (each part of the décollement is submitted to a homogeneous strain and is limited by virtual lines of strain discontinuity). (b) State at time t, where different domains can be recognized. (I) Domain that underwent only simple shear. (II) Domain that underwent firstly simple shear and then a mixed deformation regime (simultaneous pure shear and simple shear). (III) Domain that underwent only the mixed regime: pure shear and simple shear. An independent reference frame is defined for each part of the décollement. Thus ($X1$, $Y1$), ($X2$, $Y2$) and ($X3$, $Y3$) are local frames of reference for the basal flat, the ramp and the second flat, respectively. H is the initial thickness of the ductile horizon and $R(t)$ is the displacement in the basal flat at time t.

the different parts of the décollement. This is consistent with observations made by Malavieille & Ritz (1989) on ductile deformation in Triassic evaporitic décollements.

In the initial basal flat we assume simple shear deformation (Fig. 2, part 1). We refer here to the model presented by Ramsay & Graham (1970) and the review by Sanderson (1982) on models of strain variation in nappes and thrust sheets, where deformation corresponds to a simple shear if there is no volume change. For this case

Table 1. Parameters

t	time
$D(t)_{ij}$	linear transformation tensor between initial and final stages
H	thickness of the ductile layer
$R(t)$	total displacement on the décollement
α	ramp angle
β	$(\pi - \alpha)/2$
$\gamma_{BF}(t)$	shear value on the basal flat at time t
$\begin{pmatrix} P_1 & P_2 \\ P_2 & P_3 \end{pmatrix}$	symmetric component of tensor D_{ij} (pure shear)
ψ	rotation angle defining the rigid body rotation component of the tensor D_{ij}
S_{max}	maximum stretch
θ_f	angle between the ramp and the greatest principal axis of the finite strain ellipse
θ_i	angle between the ramp and the greatest principal axis of the finite strain ellipse in the initial stage

$$D(t)_{11} = 1 \tag{2}$$

$$D(t)_{12} = \frac{R(t)}{H} \tag{3}$$

$$D(t)_{21} = 0 \tag{4}$$

$$D(t)_{22} = 1. \tag{5}$$

On the ramp we assume a mixed deformation regime (simultaneous simple shear and pure shear). The equations defining the transformation matrix $D(t)_{ij}$ in the ramp, can be deduced from the known initial and final co-ordinates of points A and B (Fig. 2, part 2).

$$D(t)_{11} = 1 + \gamma_{BF}(t) \cdot \sin \alpha \tag{6}$$

$$D(t)_{12} = \frac{D(t)_{11}}{\sin \alpha} - \frac{D(t)_{11}}{\tan \beta} - \frac{1}{D(t)_{11} \cdot \tan \phi} \tag{7}$$

$$D(t)_{21} = 0 \tag{8}$$

$$D(t)_{22} = \frac{1}{D(t)_{11}}, \tag{9}$$

where

$$\gamma_{BF}(t) = \frac{R(t)}{H}$$

$$\tan \phi = \frac{1}{\gamma_{BF}(t) + \dfrac{1}{\sin \alpha} - \dfrac{1}{\tan \beta}}.$$

$\gamma_{BF}(t)$ is the shear strain on the basal flat at time t, H is the initial thickness of the décollement level and $R(t)$ is the displacement in the basal flat at time t (Fig. 2b).

We assume that the magnitude of the total displacement along the décollement is equal to the displacement in the basal flat, $R(t)$ (Fig. 2b). This condition fits many ramp flat structures as shown by Chapman & Williams (1984). Nevertheless, this paper does not attempt to describe the deformation regime, outside the ductile level.

We also assume that there is no slip between the ductile level and rigid adjacent levels, and no gradual transition from the flat strain regime to the ramp strain regime (Fig. 2). This simplifies the problem: a transitional regime could be calculated but it would not change the main results of the study.

The results will be discussed in terms of different strain parameters related to the greatest principal axis of the strain ellipse. Therefore it is convenient to subdivide the homogeneous transformation between the initial and the final stages into a rigid-body rotation and a pure strain (Germain 1986):

$$\begin{pmatrix} D_{11} & D_{12} \\ 0 & D_{22} \end{pmatrix} = \begin{pmatrix} P_1 & P_2 \\ P_2 & P_3 \end{pmatrix} \begin{pmatrix} +\cos \psi & \sin \psi \\ -\sin \psi & \cos \psi \end{pmatrix}, \tag{10}$$

where

$$\tan \psi = \frac{D_{12}}{D_{11} + D_{22}} \tag{11}$$

$$P_3 = D_{22} \cdot \cos \psi \tag{12}$$

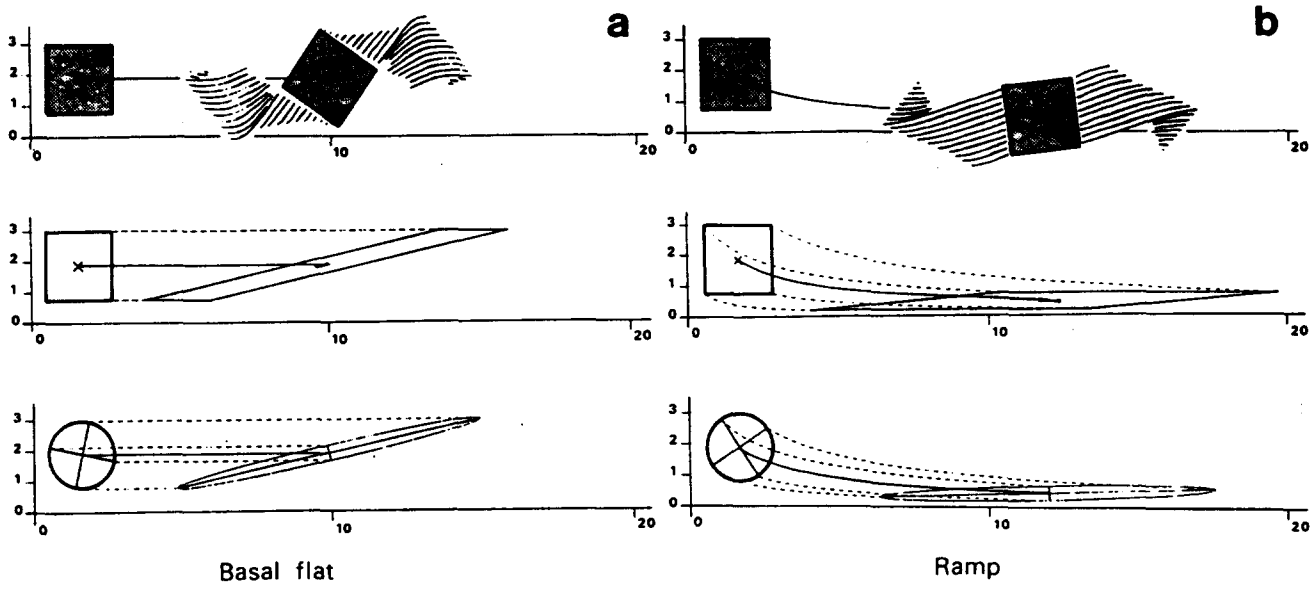

Fig. 3. Deformation paths and finite strains of rigid objects and matrix elements with respect to a local reference frame, the origin of which coincides with a material point in the matrix. Finite shear value on the basal flat is $\gamma_{BF} = 4.41$. Comparison between the flat (a) and the ramp (b). Top: pressure shadows around square rigid object. Middle: deformation of a square element in a ductile matrix. Bottom: strain ellipse and deformation path of finite principal axes.

$$P_2 = P_3 \cdot \tan \psi \tag{13}$$

$$P_1 = \frac{(D_{11} + P_2 \cdot \sin \psi)}{\cos \psi}. \tag{14}$$

The strain parameters considered in this study are as follows.

The maximum stretch

$$S_{max} = \frac{P_1 + P_3 + \sqrt{(P_1 + P_3)^2 + 4(P_2^2 - P_1 P_3)}}{2}. \tag{15}$$

The angle between the ramp and the greatest principal axis of the finite strain ellipse

$$\theta_f = \arctan\left(\frac{S_{max} - P_1}{P_2}\right). \tag{16}$$

The angle between the ramp and the greatest principal axis of the strain ellipse in the initial state θ_i (anticlockwise angles for θ_i and θ_f are defined as positive).

The clockwise rotation of the greatest principal axis of the strain ellipse

$$\psi = \theta_i - \theta_f. \tag{17}$$

RESULTS

To illustrate the different deformation paths, pressure shadows around rigid objects have been simulated for the ramp geometry represented in Fig. 1. We have considered two square objects localized, respectively, near the future ramp and in the initial flat (Fig. 1a), at time $t = 0$. These two objects are submitted to different homogeneous strain histories. The finite shear value on the basal flat is $\gamma_{BF} = 4.41$ (Fig. 1c). The case of an object undergoing a combination of the two histories (domain II in Fig. 2b) is omitted in order to simplify the results.

The comparison between the deformation path on the ramp and in the initial flat is represented in Fig. 3. The pressure shadows around the object submitted to ramp deformation (Fig. 3b, top) are more elongated and indicate less rotation than those of the object submitted to simple shear (basal flat deformation) (Fig. 3a, top).

The finite strain ellipses show the difference in rotation and flattening in the matrix between the two deformation regimes (Fig. 3, bottom). The stretch S_{max} and rotation ψ of the greatest principal axis are $S_{max} = 4.98$ and $\psi = 32.7°$ for the ramp deformation, whereas $S_{max} = 4.63$ and $\psi = 65.6°$ for the basal flat deformation.

We can extend these results by calculating the parameters defined previously (ψ, S_{max}, θ_i, θ_f) as a function of the dip of the ramp α, at different times (Fig. 4). Thus the rotation ψ of the greatest principal axis is strongly dependent on the ramp dip α and tends asymptotically with time to $\psi = 90° - \alpha$. For small dips, the rotation angle increases rapidly with time; for steeper angles, rotation increases smoothly with time and can be antithetic with respect to the shear sense (Fig. 4a). The stretch S_{max} of the principal axis is slightly higher for steep dip angles than for low dip angles. Moreover, its rate of change, $\partial S_{max}/\partial t$, increases with time (Fig. 4b). The parameter θ_i varies in an almost linear way with respect to the dip α and its behaviour is similar to that of the rotation ψ as time increases (Fig. 4c). On Fig. 4(d) it is shown that θ_f is maximum and equal to 45° for $\alpha = 0$ and $t = \Delta t$ (simple shear case), and decreases with α. Thus, the ellipse becomes parallel to the ramp as time increases.

APPLICATION OF THE MODEL

One of the possible applications of the model is the determination of the ramp dip and the shear value on the basal flat from pressure shadow data. These results can constrain the construction of cross-sections. To illustrate this, we have chosen a field example of a décollement situated in front of the arc de Digne nappe (Southern Alps of France), for which data on numerical simulation of pressure shadows are available (Malavieille & Ritz 1989). The finite coaxial stretch parallel to the shear plane and the finite shear given from the best sample of that study are, respectively, $K_{f_2} = 8.07$ and $\gamma_f = 10.5$ (these parameters are equivalent to parameters $D(t)_{11}$ and $D(t)_{12}$ of the transformation matrix in equation 1). These values are used to determine the dip of the ramp. In Fig. 5, the parameters $D(t)_{11}$ (Fig. 5a) and $D(t)_{12}$ (Fig. 5b) have been calculated as a function of the dip of the ramp α and the time t. Horizontal lines representing the field values were plotted. The ramp angle is chosen in order to explain the field values for a fixed period of time. For this experimental case $\alpha = 34°$ and $t = 12.9$. The value of the shear strain on the basal flat is given by the intersection between the curve $D(t = 12.9)_{12}$ and the vertical axis $\alpha = 0$. For this case $\gamma_{BF} = 12.9$. This value has been imposed to a ductile level whose thickness in the basal flat ($H = 200$ m) (Fig. 6a) was estimated from stratigraphic data (geological map of the area) (Kerkhove & Roux 1974). The ramp geometry was taken from the geological cross-section, which itself takes into account the ramp angle previously deduced (Fig. 6c).

The theoretical values for the total displacement $\gamma_{BF} \cdot H_{(flat)} = 2.6$ km, and for the thickness of the ductile level in the outcrop (75 m) (Fig. 6b), are quite consistent

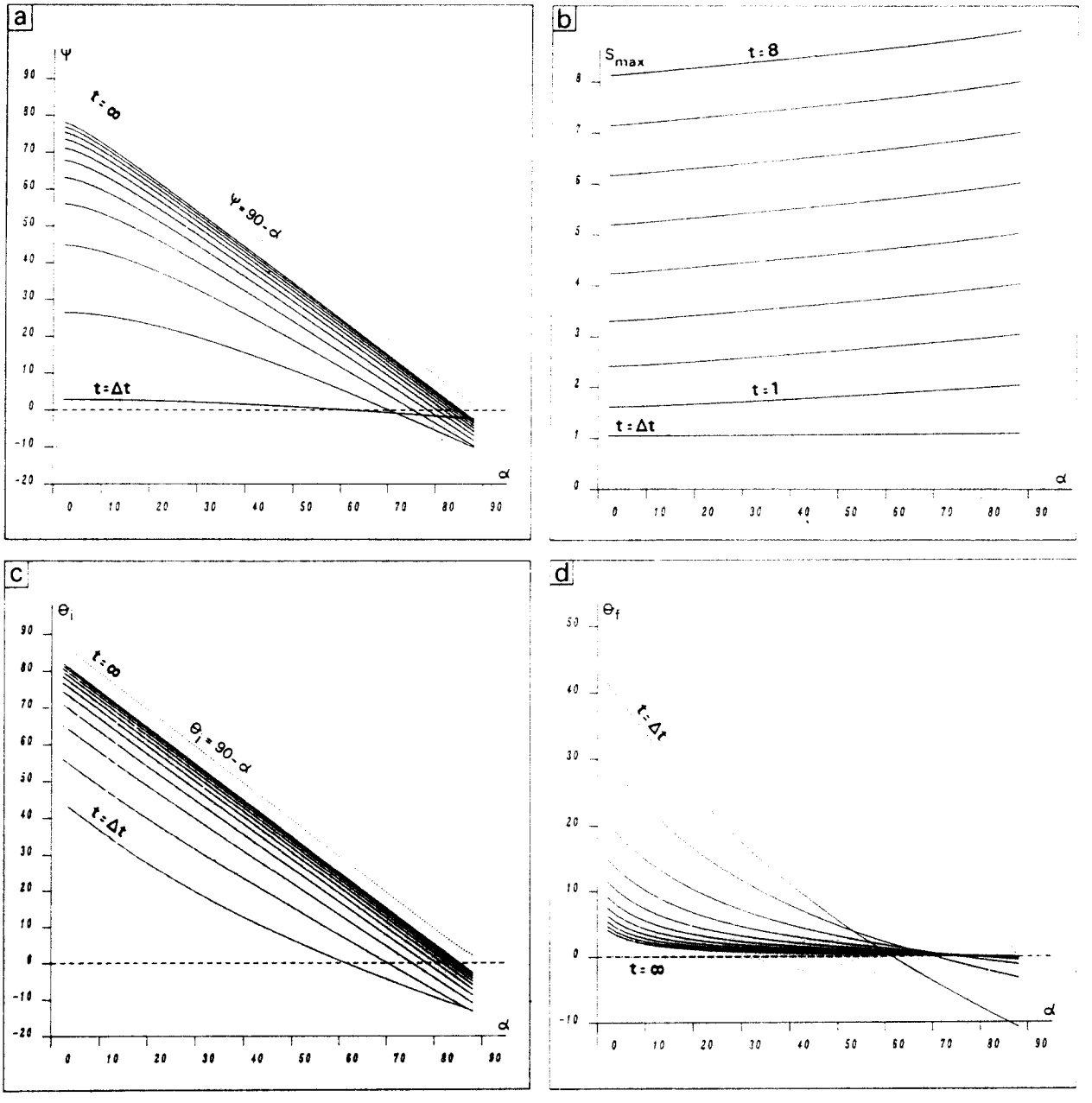

Fig. 4. Strain parameters (ψ, S_{max}, θ_i and θ_f) as a function of the dip of the ramp α at different times. The shear value per time unit is equal to 1 on the basal flat.

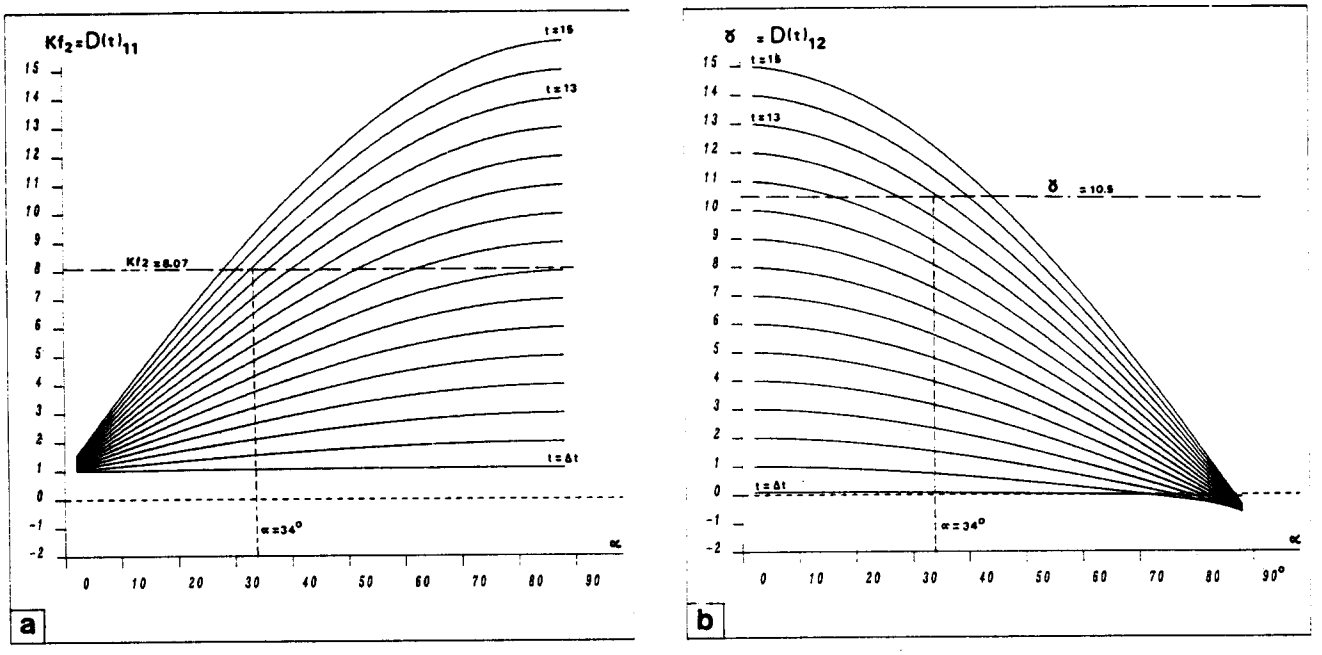

Fig. 5. Deformation parameters as a function of the dip of the ramp and time. (a) Finite coaxial stretch parallel to the shear plane; (b) finite shear. The shear value per time unit is equal to 1 on the basal flat. For the field example, the deformation parameters on the first part and the second part of the ramp are equal (Fig. 6). This condition is satisfied since the dip of the first part and the second part of the ramp are equal.

with geological data and field values (2.5 km and 50 m, respectively).

CONCLUSION

This simple theoretical kinematic model is based upon field observations which indicate that the deformation of a ductile décollement level beyond the basal flat shows more flattening and less rotation than in the simple shear case (deformation mechanism assumed in the basal flat) (Malavieille & Ritz 1989). It also makes it possible to estimate the dip of the ramp and the shear value on the basal flat from numerical simulation of observed pressure shadows. Moreover, the total displacement on the décollement can be estimated if the thickness of the ductile level is known, though it is probably underestimated since discontinuous deformation can occur in

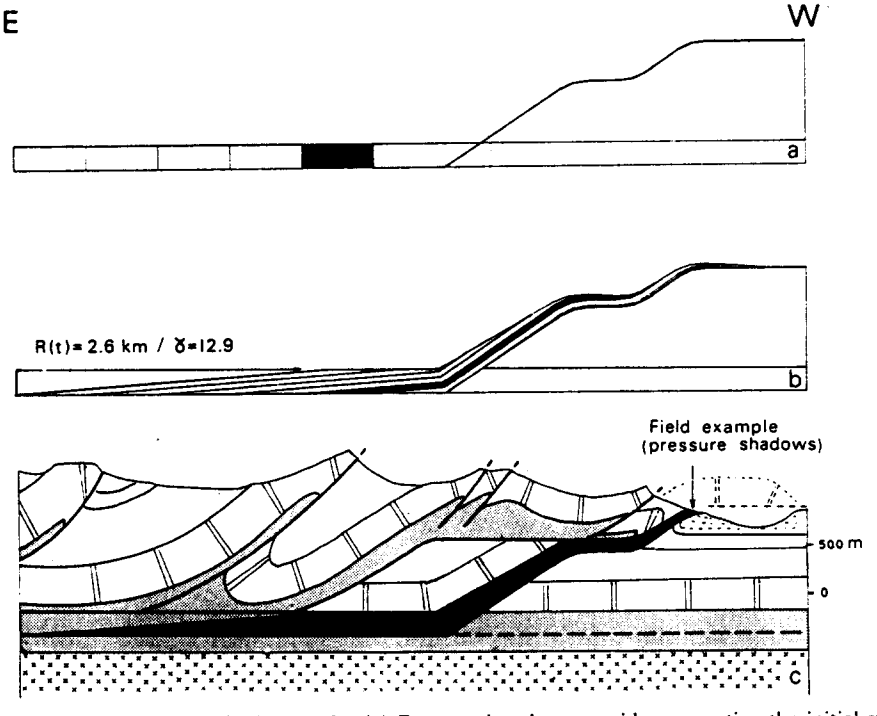

Fig. 6. Application of the model to a field example. (a) Rectangular element grid representing the initial state of the décollement level in the Triassic evaporites. (b) Finite state after imposing parameters deduced from pressure shadow data and stratigraphy. (c) Geological cross-section (after Malavieille & Ritz 1989).

addition to ductile deformation. These results can be taken into account for the construction of balanced cross-sections.

Finally, in the case where the ramp directly joins the surface from the initial flat, we can suggest that the diminution of the thickness of the plastic level is one of the factors limiting slip on the ramp.

Acknowledgements—This work has been financed by the U.R.A. 1371 CNRS.

REFERENCES

Boyer, S. E. & Elliott, D. 1982. Thrust systems. *Am. Ass. Petrol. Geol.* **66**, 1196–1230.

Butler, R. W. H. 1982. The terminology of structures in thrust belts. *J. Struct. Geol.* **4**, 239–245.

Chapman, T. J. & Williams, G. D. 1984. Displacement-distance methods in the analysis of fold-thrust structures and linked fault systems. *J. geol. Soc. Lond.* **141**, 121–128.

Davis, D. M. & Engelder, T. 1985. The role of salt in fold-and-thrust belts. *Tectonophysics* **119**, 67–88.

Eisenstadt, G. & De Paor, D. G. 1987. Alternative model of thrust-fault propagation. *Geology* **15**, 630–633.

Etchecopar, A. & Malavieille, J. 1987. Computer models of pressure-shadows: a method for strain measurement and shear-sense determination. *J. Struct. Geol.* **9**, 667–677.

Germain, P. 1986. Mécanique Tome 1. Ecole Polytechnique. *Ellipses*.

Gèze, B. 1960. La génèse néogène de l'arc de Nice (Alpes Maritimes). *C.r. somm. Soc. Géol. Fr.*, 33–34.

Kerkhove, C. & Roux, M. 1974. *Carte géologique de la France a* 1/50,000. *Moustiers-Ste-Marie, XXXIV*-42. *B.R.G.M.*

Lemoine, M. 1972. Rythmes et modalités de glissement superposés dans les chaînes subalpines méridionales des Alpes occidentales françaises. *Geol. Rdsch.* **61**, 975–1010.

Malavieille, J., Etchecopar, A. & Burg, J. P. 1982. Analyse de la géomètrie des zones abritées: simulation et application à des exemples naturels. *C.r. Acad. Sci., Paris* **294**, 279–284.

Malavieille, J. & Ritz, J. F. 1989. Mylonitic deformation of evaporites in décollements: examples from the Southern Alps in France. *J. Struct. Geol.* **11**, 583–590.

Marcoux, J., Brun, J.-P., Burg, J.-P & Ricou, L. E. 1987. Shear structures in anhydrite at the base of thrust sheets (Antalya, Southern Turkey). *J. Struct. Geol.* **9**, 555–561.

Mitra, S. 1986. Duplex structures and imbricate thrust systems: geometry, structural position, and hydrocarbon potential. *Bull. Am. Ass. Petrol. Geol.* **70**, 1087–1112.

Ramsay, J. G. & Graham, R. H. 1970. Strain variation in shear belts. *Can. J. Earth Sci.* **7**, 786–813.

Ritz, J. F. & Malavieille, J. 1988. Déformation des évaporites triasiques associées à la mise en place de diverses nappes alpines. *12ème R.S.T., Lille Soc. Géol. Fr.*, Paris, 116.

Sanderson, D. J. 1982. Models of strain variation in nappes and thrust sheets: a review. *Tectonophysics* **88**, 201–233.